RaftMLP: How Much Can Be Done Without Attention and with Less Spatial Locality?

Yuki Tatsunami Masato Taki
Rikkyo University
Toshima, Tokyo, Japan
{tatsunami, taki_m}@rikkyo.ac.jp

Abstract

For the past ten years, CNN has reigned supreme in the world of computer vision, but recently, Transformer has been on the rise. However, the quadratic computational cost of self-attention has become a serious problem in practice applications. There has been much research on architectures without CNN and self-attention in this context. In particular, MLP-Mixer is a simple architecture designed using MLPs and hit an accuracy comparable to the Vision Transformer. However, the only inductive bias in this architecture is the embedding of tokens. This leaves open the possibility of incorporating a non-convolutional (or non-local) inductive bias into the architecture, so we used two simple ideas to incorporate inductive bias into the MLP-Mixer while taking advantage of its ability to capture global correlations. A way is to divide the token-mixing block vertically and horizontally. Another way is to make spatial correlations denser among some channels of token-mixing. With this approach, we were able to improve the accuracy of the MLP-Mixer while reducing its parameters and computational complexity. The small model that is RaftMLP-S is comparable to the state-of-the-art global MLP-based model in terms of parameters and efficiency per calculation. In addition, we tackled the problem of fixed input image resolution for global MLP-based models by utilizing bicubic interpolation. We demonstrated that these models could be applied as the backbone of architectures for downstream tasks such as object detection. However, it did not have significant performance and mentioned the need for MLP-specific architectures for downstream tasks for global MLP-based models. The source code in PyTorch version is available at https://github.com/okojoalg/raft-mlp.

1. Introduction

In the past decade, CNN-based deep architectures have been developed in the computer vision domain. The first of these models was AlexNet [26], followed by other well-known models such as VGG [38], GoogLeNet [39], and ResNet [17]. These CNN-based models have exhibited high accuracy in various tasks, including image classification, object detection, semantic segmentation, and image generation. Adopting convolution, they employ the inherent inductive bias of images. Meanwhile, Transformer [48] has been winning success in recent years in the field of Natural Language Processing(NLP). Inspired by this success, Vision Transformer(ViT) [13] has been proposed. ViT is a Transformer-based visual model that replaces CNN with the self-attention mechanism. The main idea of ViT is to divide the image into patches based on their spatial locations and apply the Transformer using these patches as tokens. Immediately after the ViT paper appeared, various related works [1,4,12,14,15,33,49,53,56,58] have been done. They have shown that Transformer-based models are competitive with or even exceed CNN-based models in various image recognition and generation tasks. Although Transformer-based models have a reduced inductive bias for images compared to CNN-based models, they compensate for this lack by using a vast array of parameters and computational complexity instead. Moreover, it is successful because it can capture global correlations due to replacing the local receptive fields of convolution with global attention.

More recently, there has been a growing interest in improving the computational complexity of computationally intensive self-attention. Some works [35, 43, 44] claim that MLP alone is sufficient for image tasks without self-attention. In particular, MLP-Mixer [43] has performed a wide variety of MLP-based experiments, and the accuracy of image classification is not better than ViT, but the results are comparable. The MLP-based model, like ViT, first decomposes an image into tokens. A combined operation of MLP, transposition, and activation functions follows the tokenization. The significant point to note is that the transposition operation switches from token-mixing block to channel-mixing block and vice versa. While the channel-mixing block is equivalent to 1x1 convolution in CNN, the token-mixing block is a module that can capture the global correlations between tokens.

The wonderful thing about the MLP-Mixer is that it ex-

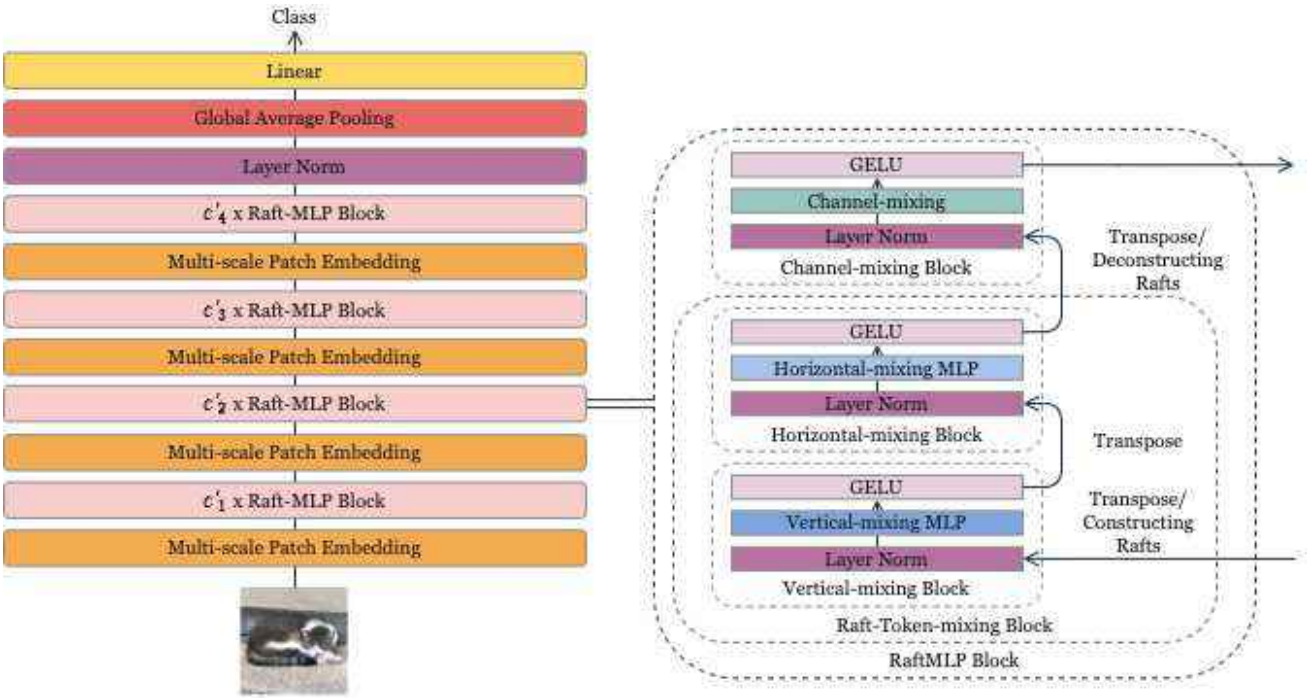

Figure 1. The whole architecture of RaftMLP

hibited the possibility of competing with the existing models with a simple architecture without convolution nor self-attention. In particular, the fact that a simple MLP-based model could compete with current models leads us to think about successors to convolution. This idea has triggered the interest of many researchers on whether computer vision tasks can outgrow the classical convolution paradigm that has been in the mainstream for ten years. Motivated by the MLP-Mixer, some architectures have been proposed that inject convolutional local structures in pursuit of accuracy. We call the models with such structures local MLP-based models. In contrast, models such as MLP-Mixer, which adopt a design to capture global correlations without local operation, are called global MLP-based models. The global MLP-based model, including MLP-Mixer, has a shortcoming with the models. Unlike convolution, the resolution of the images used for training and inference is fixed, and thwarts the application to downstream tasks such as object detection and semantic segmentation. This paper aims to achieve cost-effectiveness and ease of application to downstream tasks with fewer resources in developing a global MLP-based model. The contributions of this study are as follows.

Spatial structure As shown in Figure 1, we propose a module in which the token mixing block is divided into vertical and horizontal mixing blocks in series. In the standard MLP-Mixer, the relevance of patches has no inductive bias in the vertical and horizontal directions in the original two-dimensional image. In our proposed model, we implicitly assume as an inductive bias that patch sequences aligned horizontally have similar correlations with other horizontally aligned patch sequences. The same can be said for vertically aligned patch sequences—additionally, groups of channels are jointed in tensors before inputting into vertical-mixing and horizontal-mixing blocks. Jointed channels are shared with both mixing blocks. Thus, we assume that there is geometrical relation among some channels.

Multi-scale patch embedding While ViT and MLP-Mixer patch embedding was a simple method; we added a hierarchical structure. That is multi-scale patch embedding, which embeds information around the patch in the original patch embedding, as shown in Figure 3. The multi-scale patch embedding method, which also embeds information around the patch in the embedding of the original patch, helped us increase the accuracy at the cost of a small amount of computation and memory consumption.

Support for images of any resolution By sandwiching the bicubic interpolation before and after the token-mixing block, global MLP-based models support images of arbitrary resolution like CNNs. In addition to this contribution, we were able to apply the global MLP-based model to downstream tasks.

We will demonstrate that the proposed model with a

simple inductive bias without excessive spatial locality as convolution is superior to MLP-Mixer and comparable to global MLP-based models. In addition, we will mention that the proposed method is a model that can achieve accuracy at a reduced cost compared to previous studies. We will show the applicability of the proposed model to downstream tasks such as semantic segmentation, instance segmentation, and object detection. The results will encourage the future possibilities of architectures without self-attention and with less spatial locality.

2. Related Work

Transformer-based models Originally proposed for NLP, Transformer [48] soon began to be applied to other domains, including visual tasks. In particular, in image recognition, the attention-augmented convolution has been introduced in [3, 21, 51]. Stand-alone attention for visual task, rather than an augmentation to convolution, is studied in [37], where it was shown that fully self-attentional version of ResNet-50 outperforms the original ResNet in ImageNet classification task.

More Transformer-like architectures that process input tokens by self-attention, rather than augmenting CNNs by attention, were studied in [8, 13]. In particular, in [13], ViT based on a BERT-type pure Transformer was proposed to deal with high-resolution inputs such as the ImageNet dataset. ViT was pre-trained using a large-scale dataset and transferred to ImageNet, which gave superior results compared to state-of-the-art CNNs.

Inspired by ViT, various transformer-like architectures have been proposed. The most relevant one to our study is CrossFormer [50], which includes a hierarchical structure and Cross-scale Embedding for patch embedding at each level. Cross-scale Embedding effectively injects inductive biases for image domain by using convolution with multiple kernel sizes to perform patch embedding, and it resembles our proposed Multi-scale Patch Embedding in the basic idea. In addition, CrossFormer also proposes a method called Long Short Distance Attention, in which self-attention is divided into two parts, one for long-distance and one for short-distance.

Grobal MLP-based models Recently, several alternatives to CNN-based architectures have been proposed that are simple, yet competitive with CNN despite not using convolution or self-attention [35, 43, 44]. MLP-Mixer [43] replaces the self-attention layer of ViT with simple cross-tokens MLP. Despite its simplicity, MLP-Mixer achieves results that are competitive with ViT. gMLP [32] which consists of an MLP-based module with multiplicative gating is an alternative to MLP-Mixer, achieves higher accuracy than MLP-Mixer with fewer parameters. Vision Permutator [19] focused on mixing in vertical and horizontal directions like our work. Unlike ours, which employs a serialized structure, the Vision Permutator incorporates a parallelized structure, which results in higher accuracy with fewer parameters than the MLP-Mixer.

Local MLP-based models Moving to a generic inductive bias like Transformer and MLP has attractive possibilities, but its lack of an inductive bias like convolution means that its pre-training requires vast amounts of data compared to CNNs. In order to achieve good performance without large datasets, MLP-based architectures have been proposed as an alternative to MLPs such as S^2-MLP [52], AS-MLP [28], CycleMLP [6], and ConvMLP [27], which incorporate local structures. Although these models have the name of MLP, their essential motivation is the same as CNN in that they use the local structure of the models to extract patterns efficiently. Hence, we call these MLP-based architectures local MLP-based models. In contrast, architectures that mainly utilize MLPs to capture global correlations, such as MLP-Mixer and our study, is called global MLP-based models.

3. RaftMLP

In this section, we describe MLP-Mixer on which RaftMLP is based and the method adopted for RaftMLP.

3.1. Background

MLP-Mixer [43] splits an inputted image into patches of the same size immediately after input and is followed by MLPs that maintain the patch structure. There are two types of MLP: The first one is the token-mixing block, another is the channel-mixing block. We split an image with height h and width w into tokens with height and width p. If h and w are divisible by p, by viewing this image as a collection of these tokens, we can regard the image as an data array of height $h' = h/p$, width $w' = w/p$ and channel cp^2 where c denotes channel of the inputted image. The number of a token is then $s = hw/p^2$. The token-mixing block is map $\mathbb{R}^s \to \mathbb{R}^s$ that acts across axes of a token. In contrast, the channel-mixing block is map $\mathbb{R}^c \to \mathbb{R}^c$ that acts across axes of a channel as well where c is the number of channels. Both blocks contain the same modules: Layer Normalization(LN) [2] for each channel, Gaussian Error Linear Units(GELU) [18] and MLP. Concretely, the following equation gives the blocks

$$\mathbf{X}_{\text{output}} = \mathbf{X}_{\text{input}} + W_2\texttt{GELU}(W_1\texttt{LN}(\mathbf{X}_{\text{input}})), \quad (1)$$

where $\mathbf{X}_{\text{input}}$ denotes input tensor, $\mathbf{X}_{\text{output}}$ denotes output tensor, $W_1 \in \mathbb{R}^{a\times ae}, W_2 \in \mathbb{R}^{ae\times a}$ denote matrices of MLP layer, and e_a denotes expansion factor. For simplicity, the bias term in MLP was omitted. In token-mixing block, $a = s$ and in channel-mixing block, $a = c$. Moreover, the token-axis and channel-axis are permuted between both mixings.

In this way, MLP-Mixer [43] is composed of transposition and two types of mixing blocks.

3.2. Vertical-mixing and Horizontal-mixing Block

In the previous subsection, we discussed the token-mixing block. The original token-mixing block does not reflect any two-dimensional structure of an input image, such as height or width direction. In other words, the inductive bias for images is not included in the token-mixing block. MLP-Mixer [43] therefore has no inductive bias for images except for how the first patches are made. We decompose this token-mixing block into two blocks that mix vertical and horizontal axes respectively and incorporate inductive bias for image domain. The following describes our method.

The vertical-mixing block is map $\mathbb{R}^{h'} \to \mathbb{R}^{h'}$ that acts across the vertical axis. Precisely, this map captures correlations along the horizontal axis, utilizing the same MLP along the channel and horizontal dimensions. The map also applies layer normalization for each channel, GELU, and the residual connection. The components of this mixing block are the same as the original token-mixing block.

Similarly, the horizontal-mixing block is map $\mathbb{R}^{w'} \to \mathbb{R}^{w'}$, and shuffle the horizontal axis. The structure is dual, only replacing vertical and horizontal axes. We propose replacing token-mixing with a successive application of vertical-mixing and horizontal-mixing, assuming meaningful correlations along vertical and horizontal directions of 2D images. This structure is shown in Figure 1. The formula is as follows:

$$\begin{aligned}\mathbf{U}_{*,j,k} =& \mathbf{X}_{*,j,k} + W_{2,\mathrm{ver}}\mathtt{GELU}(W_{1,\mathrm{ver}}\mathtt{LN}(\mathbf{X}_{*,j,k})),\\ & \forall j = 1,\dots,w',\ \forall k = 1,\dots,c, \qquad (2)\\ \mathbf{Y}_{i,*,k} =& \mathbf{U}_{i,*,k} + W_{2,\mathrm{hor}}\mathtt{GELU}(W_{1,\mathrm{hor}}\mathtt{LN}(\mathbf{U}_{i,*,k})),\\ & \forall i = 1,\dots,h',\ \forall k = 1,\dots,c, \qquad (3)\end{aligned}$$

where $W_{1,\mathrm{ver}} \in \mathbb{R}^{h'\times h'e}$, $W_{2,\mathrm{ver}} \in \mathbb{R}^{h'e\times h'}$, $W_{1,\mathrm{hor}} \in \mathbb{R}^{w'\times w'e}$, and $W_{2,\mathrm{hor}} \in \mathbb{R}^{w'e\times w'}$ denote MLP weight matrices and $\mathbf{U}$, $\mathbf{X}$, and $\mathbf{Y}$ denote feature tensors.

3.3. Channel Raft

Let us assume that several groups of feature map channels have correlations originating from spatial properties. Under this assumption, some feature maps would have some patterns across vertical or horizontal directions. To capture such spatial correlations, we integrate feature maps into the vertical and horizontal shuffle. As shown in Figure 2, this can be carried out by arranging the feature maps in $h'r \times w'r$, which is reshaping the $h' \times w' \times c$ tensor into a $h'r \times w'r \times c'$ tensor with $c' = c/r^2$ channels. We then perform the vertical-mixing and the horizontal-mixing blocks for this new tensor. In this case, the layer normalization done in each mixing is for the original channel. We refer to this structure as channel raft. The combination of vertical- and horizontal-mixing blocks and the channel raft is called raft-token-mixing block in this paper. The pseudo-code for the raft-token-mixing block is given in Appendix A.1. The combination of raft-token-mixing block and the channel-mixing block is referred to as RaftMLP block.

3.4. Multi-scale Patch Embedding

The majority of both Transformer-based models and MLP-based models are based on patch embedding. We propose an extension of this method named multi-scale patch embedding, which is a patch embedding method that better represents the layered structure of an image. The main idea of the proposed method is twofold. The first is to cut out patches in such a way that the regions overlap. The second is to concatenate the channels of multiple-size patches and then project them by a linear embedding layer. The outline of the method is shown in Figure 3, and the details are explained below. First, let r be an arbitrary even number. The method performs zero-padding of $(2^m-1)r/2$ width on the top, bottom, left, and right sides then cut out the patch with $2^m r$ on one side and r stride. In the case of $m = 0$, the patch is cut out the same way as in conventional patch embedding. After this patch embedding, the height $h' = h/p$ and width $w' = w/p$ of the tensor is the same, and the output channel is $2^{2m}r^2$. Here described the implementation of multi-scale patch embedding.

Multi-scale patch embedding is a generalization of conventional patch embedding, but it is also slightly different from convolution. However, by injecting a layered structure into the embedding, it can be said to incorporate the inductive bias for images. As the m increases, the computational complexity increases, so we should be careful to decide which m patch cutout to use. Our method is similar to convolutional embedding, but it slightly differs because it uses a linear layer projection after concatenating. See Appendix A.1 for code details.

3.5. Hierarchical Design

In the proposed method, hierarchical design is introduced. Our architecture used a four-level hierarchical structure with channel raft and multi-scale patch embedding to effectively reduce the number of parameters and improve the accuracy. The hierarchical design is shown in Figure 1. In this architecture, the number of levels is $L = 4$, and at level l, after extracting a feature map of $h/2^{l+1} \times w/2^{l+1} \times c_l$ by multi-scale patch embedding, the RaftMLP block is repeated k_l times. The embedding is done using multi-scale patch embedding, but for $l = 1, 2, 3$, the feature maps for $m = 0, 1$ are concatenated, and for $l = 4$, conventional patch embedding is used. We prepared a hierarchical RaftMLP model with multiple scales. By settling c'_l, the number of channels for the level l, and

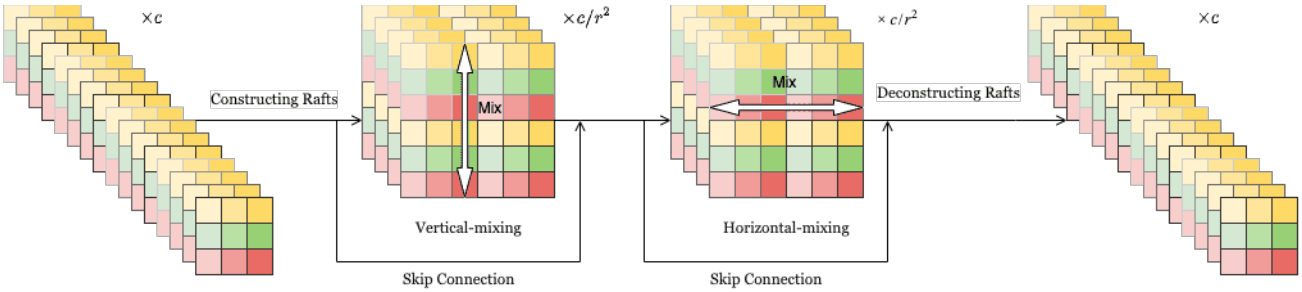

Figure 2. The architecture of the raft-token-mixing block. Channels are rearranged with raft-like structure, and then vertical and horizontal mixed.

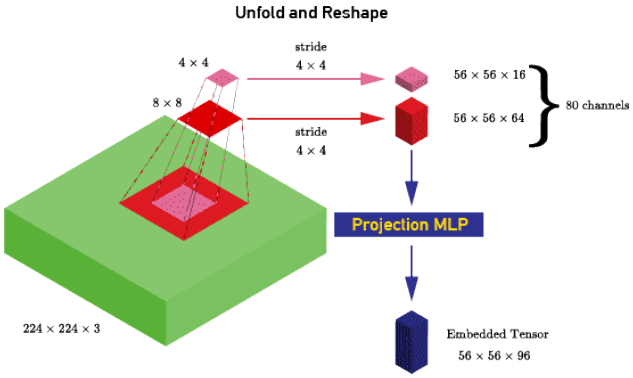

Figure 3. A visualization of the concept of multi-scale-embedding.

N_l, the number of RaftMLP blocks for the level, we developed models for three scales: **RaftMLP-S**, **RaftMLP-M**, and **RaftMLP-L**. The common settings for all three models are vertical dilation expansion factor $e_{\text{ver}} = 2$, horizontal dilation expansion factor $e_{\text{hor}} = 2$, channel dilation expansion factor $e_{\text{can}} = 4$, and channel raft size $r = 2$. For patch embedding at each level, multi-scale patch embedding is utilized, but for the $l = 1, 2, 3$ level, patch cutting is performed for $m = 0, 1$ and then concatenated. For the final level, conventional patch embedding to reduce parameters and computational complexity is utilized. For the output head, a classifier with linear layers and softmax is applied after global average pooling. Refer to Table 5 for other settings. Our experiments show that the performance of image classification improves as the scale is increased.

3.6. Impact of Channel Raft on Computational Costs

We will discuss the computational complexity of channel raft, ignoring normalization and activation functions. Here, let h' denote the height of the patch placement, w' the width of the patch placement, and e the expansion factor.

Number of parameters The MLPs parameter for a conventional token-mixing block is

$$h'w'(2eh'w' + e + 1). \tag{4}$$

In contrast, the parameter used for a vertial-mixing block is

$$h'r(2eh'r + e + 1), \tag{5}$$

and the parameter used for a holizonal-mixing block is

$$w'r(2ew'r + e + 1). \tag{6}$$

In other words, the total number of parameters required for a raft-token-mixing block is

$$h'r(2eh'r + e + 1) + w'r(2ew'r + e + 1). \tag{7}$$

This means that if we assume $h' = w'$ and ignore $e + 1$, the parameters required for a conventional token-mixing block in the proposed method are $2(r/h')^2$ times for a conventional token-mixing. In short, if we choose r to satisfy $r < h'/\sqrt{2}$, the memory cost can be reduced.

Number of multiply-accumulate If we ignore the bias term, the MLPs used for a conventional token-mixing block require $e(h'w')^4$ multiply-accumulates. By contrast, a raft-token-mixing block requires only $er^4(h'^4 + w'^4)$. Assuming $h' = w'$, a raft-token-mixing requires only multiply-accumulate of $2r^4/h'^4$ ratio to conventional token-mixing block. To put it plainly, if r is chosen so that $r < h'/2^{\frac{1}{4}}$, then multiply-accumulation has an advantage over a conventional token-mixing block.

3.7. Downstream Task Application

In order to apply our models to downstream tasks such as semantic segmentation, instance segmentation, and object detection, various resolutions need to be supported. Therefore, we insert bicubic interpolation before and after the raft-token-mixing block, as shown in Figure 4. In the bicubic interpolation before the block, we convert the input to

the resolution used for pre-training. The bicubic interpolation after the block restores the resolution before the first bicubic interpolation. Moreover, since the resolution of input images is not always divisible by the patch size, we apply bicubic interpolation to obtain the resolution before multi-scale embedding that is a factor of the patch size. This method can be applied to other global MLP-based models such as MLP-Mixer too.

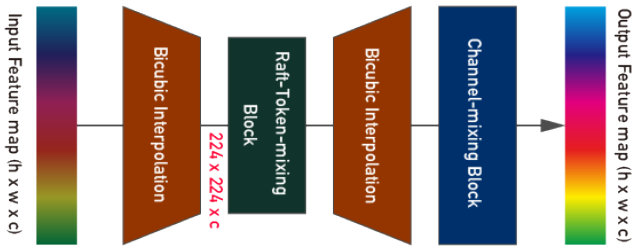

Figure 4. Application of RaftMLP block utilizing bicubic interpolation

4. Experimental Evaluation

In this section, we exhibit experiments for image classification with RaftMLP. In the principal part of this experiment, we utilize the Imagenet-1k dataset [10] to train three types of RaftMLP and compare them with MLP-based models and Transformers-based models mainly. We also carry out an ablation study to demonstrate the effectiveness of our proposed method, and as a downstream task, we evaluate transfer learning of RaftMLP for image classification. Besides, We conduct experiments employing RaftMLP as the backbone for object detection and semantic segmentation.

4.1. ImageNet-1k

To evaluate the training results of our proposed classification models, RaftMLP-S, RaftMLP-M and RaftMLP-L, we train them on ImagNet-1k dataset [10]. This dataset consists of about 1.2 million training images and about 50,000 validation images assigned 1000 category labels. We also describe how the training is set up below. We employ AdamW [34] with weight decay 0.05 and learning schedule: maximum learning rate $\frac{\text{batch size}}{512} \times 5 \times 10^{-4}$, linear warmup on first 5 epochs, and after cosine decay to 10^{-5} on the following 300 epochs to train our models. Moreover, we adopt some augmentations and regularizations; random horizontal flip, color jitter, Mixup [55] with $\alpha = 0.8$, CutMix [54] with $\alpha = 1.0$, Cutout [11] of rate 0.25, RandAugment [9], stochastic depth [22] of rate 0.1, and label smoothing [40] 0.1. These settings refer to the training strategy of DeiT [45]. The other settings are changed for each experiment. Additionally, all training in this experiment is performed on a Linux machine with 8 RTX Quadro 8000 cards. The results of trained models are showed in Table 1. In Figure 5, we compare our method with other global MLP-based models in terms of accuracy against the number of parameters and computational complexity. Figure 5 reveals that RaftMLP-S is a cost-effective method.

Table 1. Accuracy of the models to be compared with the accuracy of the models derived from the experiments with ImageNet-1k

Backbone	Model	#params (M)	FROPs (G)	Top-1 Acc.(%)	Top-5 Acc.(%)
Low-resource Models (#params × FLOPs less than 50P)					
CNN	ResNet-18 [17]	11.7	1.8	69.8	89.1
	MobileNetV3 [20]	5.4	0.2	75.2	-
	EfficientNet-B0 [41]	5.3	0.4	77.1	-
Local MLP	CycleMLP-B1 [6]	15.2	2.1	78.9	-
	ConvMLP-S [27]	9.0	2.4	76.8	-
Global MLP	ResMLP-S12 [44]	15.4	3.0	76.6	-
	gMLP-Ti [32]	6.0	1.4	72.3	-
	RaftMLP-S (**ours**)	9.9	2.1	76.1	93.0
Middle-Low-resource Models (#params × FLOPs more than 50P and less than 150P)					
CNN	ResNet-50 [17]	25.6	3.8	76.3	92.2
	EfficientNet-B4 [41]	19.0	4.2	82.6	96.3
Transformer	DeiT-S [45]	22.1	4.6	81.2	-
	T2T-ViT$_t$-14 [53]	21.5	6.1	81.7	-
	TNT-S [15]	23.8	5.2	81.5	95.7
	CaiT-XS24 [46]	26.6	5.4	81.8	-
	Nest-T [56]	17.0	5.8	81.5	-
Local MLP	AS-MLP-Ti [28]	28.0	4.4	81.3	-
	ConvMLP-M [27]	17.4	3.9	79.0	-
Global MLP	Mixer-S/16 [43]	18.5	3.8	73.8	-
	gMLP-S [32]	19.4	4.5	79.6	-
	ViP-Small/7 [19]	25.1	6.9	81.5	-
	RaftMLP-M (**ours**)	21.4	4.3	78.8	94.3
Middle-High-resource Models (#params × FLOPs more than 150P and less than 500P)					
CNN	ResNet-152 [17]	60.0	11.0	77.8	93.8
	EfficientNet-B5 [41]	30.0	9.9	83.7	-
	EfficientNetV2-S [42]	22.0	8.8	83.9	-
Transformer	PVT-M [49]	44.2	6.7	81.2	-
	Swin-S [33]	50.0	8.7	83.0	-
	Nest-S [56]	38.0	10.4	83.3	-
Local MLP	S^2-MLP-deep [52]	51.0	9.7	80.7	95.4
	CycleMLP-B3 [6]	38.0	6.9	82.4	-
	AS-MLP-S [28]	50.0	8.5	83.1	-
	ConvMLP-L [27]	42.7	9.9	80.2	-
Global MLP	Mixer-B/16 [43]	59.9	12.6	76.4	-
	ResMLP-S24 [44]	30.0	6.0	79.4	-
	RaftMLP-L (**ours**)	36.2	6.5	79.4	94.3
High-resource Models (Models with #params × FLOPs more than 500P)					
Transformer	ViT-B/16 [13]	86.6	55.5	77.9	-
	DeiT-B [45]	86.6	17.6	81.8	-
	CaiT-S36 [46]	68.2	13.9	83.3	-
	Nest-B [56]	68.0	17.9	83.8	-
Global MLP	gMLP-B [32]	73.1	15.8	81.6	-
	ViP-Medium/7 [19]	55.0	16.3	82.7	-

4.2. Ablation Study

In order to verify the effectiveness of the two methods we propose, we carry out ablation studies. The setup for

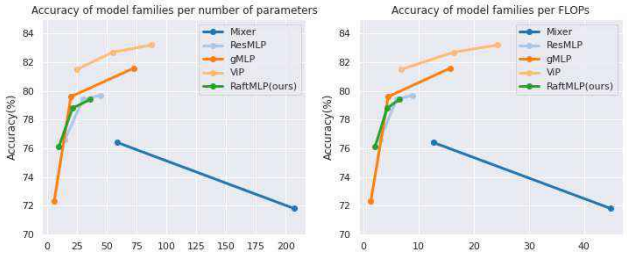

Figure 5. Accuracy per parameter and accuracy per FLOPs for the family of global MLP-based models

these experiments is the same as in Subsection 4.1.

Channel Raft(CR) We have carried out experiments to verify the effectiveness of channel rafts. Table 2 compares and verifies MLP-Mixer and MLP-Mixer with the token mixing block replaced by channel rafts. Although we have prepared architectures for $r = 1, 2, 4$ cases, $r = 1$ case has no raft structure but is just a conventional token-mixing block vertically and horizontally separated. Table 2 has shown that channel rafts effectively improve accuracy and costless channel raft structure such as $r = 2$ is more efficient for training than increasing r.

Table 2. An ablation experiment of channel raft. Note that Mixer-B/16 is experimented with our implementation

Model	r	#Mparams	GFLOPs	Top-1 Acc.
Mixer-B/16	-	59.9	12.6	74.3%
Mixer-B/16 with CR	1	58.1	11.4	77.0%
	2	58.2	11.6	78.3%
	4	58.4	12.0	78.0%

Multi-scale Patch Embedding(MSPE) RaftMLP-M is composed of three multi-scale patch embeddings and a conventional patch embedding. To evaluate the effect of multi-scale patch embedding, we compared RaftMLP-M with the model with multi-scale patch embeddings replaced by conventional patch embeddings in RaftMLP-M. The result is shown on Table 3. As a result of comparing the models with and without multi-scale patch embedding, RaftMLP-M with multi-scale patch embedding improves the accuracy by 0.7% compared to the model without multi-scale patch embedding.

Table 3. An ablation experiment of multi-scale patch embedding

Model	#Mparams	GFLOPs	Top-1 Acc.
RaftMLP-M	21.4	4.3	78.8%
RaftMLP-M without MSPE	20.0	3.8	78.1%

4.3. Transfer Learning

The study of transfer learning is conducted on CIFAR-10/CIFAR-100 [25], Oxford 102 Flowers [36], Stanford Cars [24] and iNaturalist [47] to evaluate the transfer capabilities of RaftMLP pre-trained on ImageNet-1k [10]. The fine-tuning experiments adopt batch size 256, weight decay 10^{-4} and learning schedule: maximum learning rate 10^{-4}, linear warmup on first 10 epochs, and after cosine decay to 10^{-5} on the following 40 epochs. We also do not use stochastic depth [22] and Cutout [11] in this experiment. The rest of the settings are equivalent to Subsection 4.1. In our experiments, we also resize all images to the exact resolution 224×224 as ImageNet-1k. The experiment is shown in Table 4. We achieve that RaftMLP-L is more accurate than Mixer-B/16 in all datasets.

Table 4. The accuracy of transfer learning with each dataset

Dataset	Mixer-B/16	RaftMLP-S	RaftMLP-M	RaftMLP-L
CIFAR-10	97.7%	97.4%	97.7%	98.1%
CIFAR-100	85.0%	85.1%	86.8%	86.8%
Oxford 102 Flowers	97.8%	97.1%	97.9%	98.4%
Stanford Cars	84.3%	84.7%	87.6%	89.0%
iNaturalist18	55.6%	56.7%	61.7%	62.9%
iNaturalist19	64.1%	65.4%	69.2%	70.1%

4.4. Object Detetion

For the evaluation of object detection and instance segmentation, we compose a model in which the backbones of RetinaNet [30] and Mask R-CNN [16], which are both standard implementations on the object detection framework `mmdetection` [5], are replaced by RaftMLP and MLP-Mixer. For the dataset, we used MS COCO [31], which is one of the most popular benchmark datasets for object detection. The training setup is similar to ConvMLP [27], with AdamW as the optimizer, learning rate set to 10^{-4}, weight decay set to 10^{-4}, and 12 epochs of training with a batch size of 16. The results are compared with PureMLP [27], ResNet [17, 27] and ConvMLP [27], and a summary is provided in Figure 6. See Appendix A.3 for more details.

4.5. Semantic Segmentation

We replace the backbone of the Semantic FPN [23] implemented on `mmsegmention` [7] with RaftMLP and MLP-Mixer and evaluate their performances on the segmentation task. We adopt AdamW as the optimizer with a learning rate of 2.0×10^{-4} and a weight decay of 10^{-4}. The learning schedule follows the polynomial decay learning rate policy with a power of 0.9. We use the famous ADE20K dataset [57] to train the model, with the input image randomly resized and cropped to a resolution of 512×512. The model had trained for 40000 iterations. The above settings follow ConvMLP [27]. A summary of the

experimental results is shown in Figure 6. See Appendix A.3 for more details.

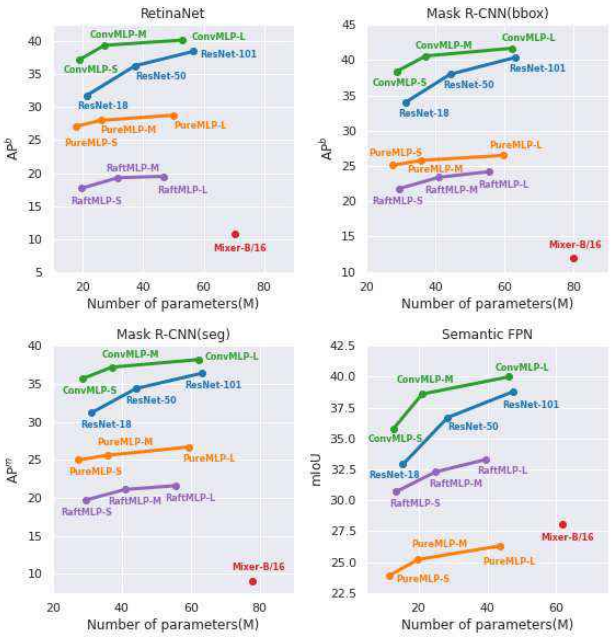

Figure 6. The above compares the training results of RetinaNet and Mask R-CNN on MS COCO and Semantic FPN on ADE20K. We compare the results with ResNet, PureMLP, ConvMLP, Mixer, and RaftMLP as backbones in each case. RetinaNet uses AP for bounding boxes, Mask R-CNN AP for bounding boxes and segmentation, and Semantic FPN uses mIoU as their metric.

5. Discussion

The above experimental results show that even an architecture that does not use convolution but has a simple inductive bias for images like vertical and horizontal decomposition can achieve performance competing with Transformers. This is a candidate for minimal inductive biases to improve MLP-based models without convolution. Also, Our method does not require as much computational cost as Transformer. In addition, the computational cost is as expensive as or less than that of CNN. The main reason for the reduced computational cost is that it does not require self-attention. The fact that only simple operations such as MLP are needed without self-attention nor convolution means that MLP-based models will be widely used in applied fields since they do not require special software or hardware carefully designed to reduce computational weight. Furthermore, the raft-token-mixing block has the lead over the token-mixing block of MLP-Mixer in terms of computational complexity when the number of patches is large. As we described in Section 3, substituting the token-mixing block as the raft-token-mixing block reduces parameters from the square of the patches to several times patches. In other words, the more the resolution of images is, the more dramatically parameters are reduced with RaftMLP. The hierarchical design adopted in this paper contributes to the reduction of parameters and computational complexity. Since multi-scale embedding leads to better performance with less cost, our proposal will make it realistic to compose architectures that do not depend on convolution. Meanwhile, the proposed model has no significant results for some downstream tasks. As shown in Appendix A.5, the feature map of global MLP-based models differs from the feature map of CNNs in that it is visualized as a different appearance from the input image. Such feature maps are not expected to work entirely in convolution-based architectures such as RetinaNet [30], Mask R-CNN [16], and Semantic FPN [23]. Global MLP-based models will require their specialized frameworks for object detection, instance segmentation, and semantic segmentation.

6. Conclusion

In conclusion, the result has demonstrated that the introduction of the raft-token-mixing block improves accuracy when trained on the ImageNet-1K dataset [10], as compared to plain MLP-Mixer [43]. Although the raft-token-mixing decreases the number of parameters and FLOPS only lightly compared to MLP-Mixer [43], it contributes to the improvement in accuracy in return. We conclude that adding a non-convolutional and non-self-attentional inductive bias to the token-mixing block of MLP-Mixer can improve the accuracy of the model. In addition, due to the introduction of hierarchical structures and multi-scale patch embedding, RaftMLP-S with lower computational complexity and number of parameters have achieved accuracy comparable to the state-of-the-art global MLP-based model with similar computational complexity and number of parameters. We have explicated that it is more cost-effective than the Transformer-based models and well-known CNNs. Furthermore, compared with the existing global MLP-based model, our method allowed an application to downstream tasks with flexible input resolution by introducing bicubic interpolation.

However, global MLP-based models have not yet fully explored their potential. The results for object detection and semantic segmentation are not as well performed as ResNet, implying the need to construct models specifically for global MLP models for each future downstream task. In addition, inducing other utilitarian inductive biases, e.g., parallel invariance, may improve the accuracy of global MLP-based models. Further insight into these aspects is left to future work.

References

[1] Anurag Arnab, Mostafa Dehghani, Georg Heigold, Chen Sun, Mario Lučić, and Cordelia Schmid. ViViT: A video vision transformer. In *ICCV*, 2021. 1

[2] Jimmy Lei Ba, Jamie Ryan Kiros, and Geoffrey E Hinton. Layer normalization. In *NeurIPS*, 2016. 3

[3] Irwan Bello, Barret Zoph, Ashish Vaswani, Jonathon Shlens, and Quoc V Le. Attention augmented convolutional networks. In *ICCV*, pages 3286–3295, 2019. 3

[4] Chun-Fu Chen, Quanfu Fan, and Rameswar Panda. CrossViT: Cross-attention multi-scale vision transformer for image classification. In *ICCV*, 2021. 1

[5] Kai Chen, Jiaqi Wang, Jiangmiao Pang, Yuhang Cao, Yu Xiong, Xiaoxiao Li, Shuyang Sun, Wansen Feng, Ziwei Liu, Jiarui Xu, Zheng Zhang, Dazhi Cheng, Chenchen Zhu, Tianheng Cheng, Qijie Zhao, Buyu Li, Xin Lu, Rui Zhu, Yue Wu, Jifeng Dai, Jingdong Wang, Jianping Shi, Wanli Ouyang, Chen Change Loy, and Dahua Lin. MMDetection: Open MMLab detection toolbox and benchmark. *arXiv preprint arXiv:1906.07155*, 2019. https://github.com/open-mmlab/mmdetection. 7

[6] Shoufa Chen, Enze Xie, Chongjian Ge, Ding Liang, and Ping Luo. CycleMLP: A MLP-like architecture for dense prediction. *arXiv preprint arXiv:2107.10224*, 2021. 3, 6

[7] MMSegmentation Contributors. MMSegmentation: Openmmlab semantic segmentation toolbox and benchmark. https://github.com/open-mmlab/mmsegmentation, 2020. 7

[8] Jean-Baptiste Cordonnier, Andreas Loukas, and Martin Jaggi. On the relationship between self-attention and convolutional layers. In *ICLR*, 2019. 3

[9] Ekin D Cubuk, Barret Zoph, Jonathon Shlens, and Quoc V Le. RandAugment: Practical automated data augmentation with a reduced search space. In *CVPR Workshops*, pages 702–703, 2020. 6

[10] Jia Deng, Wei Dong, Richard Socher, Li-Jia Li, Kai Li, and Li Fei-Fei. Imagenet: A large-scale hierarchical image database. In *CVPR*, pages 248–255, 2009. 6, 7, 8

[11] Terrance DeVries and Graham W Taylor. Improved regularization of convolutional neural networks with cutout. *arXiv preprint arXiv:1708.04552*, 2017. 6, 7

[12] Ming Ding, Zhuoyi Yang, Wenyi Hong, Wendi Zheng, Chang Zhou, Da Yin, Junyang Lin, Xu Zou, Zhou Shao, Hongxia Yang, et al. Cogview: Mastering text-to-image generation via transformers. In *NeurIPS*, 2021. 1

[13] Alexey Dosovitskiy, Lucas Beyer, Alexander Kolesnikov, Dirk Weissenborn, Xiaohua Zhai, Thomas Unterthiner, Mostafa Dehghani, Matthias Minderer, Georg Heigold, Sylvain Gelly, et al. An image is worth 16x16 words: Transformers for image recognition at scale. In *ICLR*, 2021. 1, 3, 6

[14] Alaaeldin El-Nouby, Hugo Touvron, Mathilde Caron, Piotr Bojanowski, Matthijs Douze, Armand Joulin, Ivan Laptev, Natalia Neverova, Gabriel Synnaeve, Jakob Verbeek, et al. Xcit: Cross-covariance image transformers. *arXiv preprint arXiv:2106.09681*, 2021. 1

[15] Kai Han, An Xiao, Enhua Wu, Jianyuan Guo, Chunjing Xu, and Yunhe Wang. Transformer in transformer. In *NeurIPS*, 2021. 1, 6

[16] Kaiming He, Georgia Gkioxari, Piotr Dollár, and Ross Girshick. Mask R-CNN. In *ICCV*, pages 2961–2969, 2017. 7, 8, 11

[17] Kaiming He, Xiangyu Zhang, Shaoqing Ren, and Jian Sun. Deep residual learning for image recognition. In *CVPR*, pages 770–778, 2016. 1, 6, 7, 15, 16

[18] Dan Hendrycks and Kevin Gimpel. Gaussian error linear units (GELUs). *arXiv preprint arXiv:1606.08415*, 2016. 3

[19] Qibin Hou, Zihang Jiang, Li Yuan, Ming-Ming Cheng, Shuicheng Yan, and Jiashi Feng. Vision Permutator: A permutable MLP-like architecture for visual recognition. *arXiv preprint arXiv:2106.12368*, 2021. 3, 6

[20] Andrew Howard, Mark Sandler, Grace Chu, Liang-Chieh Chen, Bo Chen, Mingxing Tan, Weijun Wang, Yukun Zhu, Ruoming Pang, Vijay Vasudevan, and Others. Searching for MobileNetV3. In *ICCV*, pages 1314–1324, 2019. 6

[21] Jie Hu, Li Shen, Samuel Albanie, Gang Sun, and Andrea Vedaldi. Gather-Excite: Exploiting feature context in convolutional neural networks. In *NeurIPS*, 2018. 3

[22] Gao Huang, Yu Sun, Zhuang Liu, Daniel Sedra, and Kilian Q Weinberger. Deep networks with stochastic depth. In *ECCV*, pages 646–661, 2016. 6, 7

[23] Alexander Kirillov, Ross Girshick, Kaiming He, and Piotr Dollár. Panoptic feature pyramid networks. In *CVPR*, pages 6399–6408, 2019. 7, 8, 11

[24] Jonathan Krause, Michael Stark, Jia Deng, and Li Fei-Fei. 3D object representations for fine-grained categorization. In *ICCV Workshops*, pages 554–561, 2013. 7

[25] Alex Krizhevsky, Geoffrey Hinton, et al. Learning multiple layers of features from tiny images. Technical report, University of Toronto, 2009. 7

[26] Alex Krizhevsky, Ilya Sutskever, and Geoffrey E Hinton. Imagenet classification with deep convolutional neural networks. In *NeurIPS*, volume 25, pages 1097–1105, 2012. 1

[27] Jiachen Li, Ali Hassani, Steven Walton, and Humphrey Shi. ConvMLP: Hierarchical convolutional MLPs for vision. *arXiv preprint arXiv:2109.04454*, 2021. 3, 6, 7, 11, 15, 16

[28] Dongze Lian, Zehao Yu, Xing Sun, and Shenghua Gao. AS-MLP: An axial shifted MLP architecture for vision. *arXiv preprint arXiv:2107.08391*, 2021. 3, 6

[29] Tsung-Yi Lin, Piotr Dollár, Ross Girshick, Kaiming He, Bharath Hariharan, and Serge Belongie. Feature pyramid networks for object detection. In *CVPR*, pages 2117–2125, 2017. 11

[30] Tsung-Yi Lin, Priya Goyal, Ross Girshick, Kaiming He, and Piotr Dollár. Focal loss for dense object detection. In *ICCV*, pages 2980–2988, 2017. 7, 8, 11

[31] Tsung-Yi Lin, Michael Maire, Serge Belongie, James Hays, Pietro Perona, Deva Ramanan, Piotr Dollár, and C Lawrence Zitnick. Microsoft COCO: Common objects in context. In *ECCV*, pages 740–755, 2014. 7

[32] Hanxiao Liu, Zihang Dai, David R So, and Quoc V Le. Pay attention to MLPs. *arXiv preprint arXiv:2105.08050*, 2021. 3, 6

[33] Ze Liu, Yutong Lin, Yue Cao, Han Hu, Yixuan Wei, Zheng Zhang, Stephen Lin, and Baining Guo. Swin transformer: Hierarchical vision transformer using shifted windows. In *ICCV*, 2021. 1, 6

[34] Ilya Loshchilov and Frank Hutter. Decoupled weight decay regularization. In *ICLR*, 2019. 6

[35] Luke Melas-Kyriazi. Do you even need attention? a stack of feed-forward layers does surprisingly well on imagenet. *arXiv preprint arXiv:2105.02723*, 2021. 1, 3

[36] Maria-Elena Nilsback and Andrew Zisserman. Automated flower classification over a large number of classes. In *ICVGIP*, pages 722–729, 2008. 7

[37] Prajit Ramachandran, Niki Parmar, Ashish Vaswani, Irwan Bello, Anselm Levskaya, and Jonathon Shlens. Stand-alone self-attention in vision models. In *NeurIPS*, 2019. 3

[38] Karen Simonyan and Andrew Zisserman. Very deep convolutional networks for large-scale image recognition. In *ICLR*, 2015. 1

[39] Christian Szegedy, Wei Liu, Yangqing Jia, Pierre Sermanet, Scott Reed, Dragomir Anguelov, Dumitru Erhan, Vincent Vanhoucke, and Andrew Rabinovich. Going deeper with convolutions. In *CVPR*, pages 1–9, 2015. 1

[40] Christian Szegedy, Vincent Vanhoucke, Sergey Ioffe, Jon Shlens, and Zbigniew Wojna. Rethinking the inception architecture for computer vision. In *CVPR*, pages 2818–2826, 2016. 6

[41] Mingxing Tan and Quoc Le. EfficientNet: Rethinking model scaling for convolutional neural networks. In *ICML*, pages 6105–6114, 2019. 6

[42] Mingxing Tan and Quoc V Le. EfficientNetV2: Smaller models and faster training. In *ICML*, 2021. 6

[43] Ilya Tolstikhin, Neil Houlsby, Alexander Kolesnikov, Lucas Beyer, Xiaohua Zhai, Thomas Unterthiner, Jessica Yung, Daniel Keysers, Jakob Uszkoreit, Mario Lucic, et al. Mlp-mixer: An all-mlp architecture for vision. *arXiv preprint arXiv:2105.01601*, 2021. 1, 3, 4, 6, 8, 15, 16

[44] Hugo Touvron, Piotr Bojanowski, Mathilde Caron, Matthieu Cord, Alaaeldin El-Nouby, Edouard Grave, Armand Joulin, Gabriel Synnaeve, Jakob Verbeek, and Hervé Jégou. Resmlp: Feedforward networks for image classification with data-efficient training. *arXiv preprint arXiv:2105.03404*, 2021. 1, 3, 6

[45] Hugo Touvron, Matthieu Cord, Matthijs Douze, Francisco Massa, Alexandre Sablayrolles, and Hervé Jégou. Training data-efficient image transformers & distillation through attention. In *ICML*, 2021. 6

[46] Hugo Touvron, Matthieu Cord, Alexandre Sablayrolles, Gabriel Synnaeve, and Hervé Jégou. Going deeper with image transformers. In *ICCV*, pages 32–42, 2021. 6

[47] Grant Van Horn, Oisin Mac Aodha, Yang Song, Yin Cui, Chen Sun, Alex Shepard, Hartwig Adam, Pietro Perona, and Serge Belongie. The iNaturalist species classification and detection dataset. In *CVPR*, pages 8769–8778, 2018. 7

[48] Ashish Vaswani, Noam Shazeer, Niki Parmar, Jakob Uszkoreit, Llion Jones, Aidan N Gomez, Lukasz Kaiser, and Illia Polosukhin. Attention is all you need. In *NeurIPS*, 2017. 1, 3

[49] Wenhai Wang, Enze Xie, Xiang Li, Deng-Ping Fan, Kaitao Song, Ding Liang, Tong Lu, Ping Luo, and Ling Shao. Pyramid vision transformer: A versatile backbone for dense prediction without convolutions. In *ICCV*, 2021. 1, 6

[50] Wenxiao Wang, Lu Yao, Long Chen, Deng Cai, Xiaofei He, and Wei Liu. CrossFormer: A versatile vision transformer based on cross-scale attention. *arXiv preprint arXiv:2108.00154*, 2021. 3

[51] Xiaolong Wang, Ross Girshick, Abhinav Gupta, and Kaiming He. Non-local neural networks. In *CVPR*, pages 7794–7803, 2018. 3

[52] Tan Yu, Xu Li, Yunfeng Cai, Mingming Sun, and Ping Li. S^2-MLP: Spatial-shift MLP architecture for vision. *arXiv preprint arXiv:2106.07477*, 2021. 3, 6

[53] Li Yuan, Yunpeng Chen, Tao Wang, Weihao Yu, Yujun Shi, Francis EH Tay, Jiashi Feng, and Shuicheng Yan. Tokens-to-Token ViT: Training vision transformers from scratch on ImageNet. In *ICCV*, pages 558–567, 2021. 1, 6

[54] Sangdoo Yun, Dongyoon Han, Seong Joon Oh, Sanghyuk Chun, Junsuk Choe, and Youngjoon Yoo. Cutmix: Regularization strategy to train strong classifiers with localizable features. In *ICCV*, pages 6023–6032, 2019. 6

[55] Hongyi Zhang, Moustapha Cisse, Yann N Dauphin, and David Lopez-Paz. mixup: Beyond empirical risk minimization. In *ICLR*, 2018. 6

[56] Zizhao Zhang, Han Zhang, Long Zhao, Ting Chen, and Tomas Pfister. Aggregating nested transformers. *arXiv preprint arXiv:2105.12723*, 2021. 1, 6

[57] Bolei Zhou, Hang Zhao, Xavier Puig, Sanja Fidler, Adela Barriuso, and Antonio Torralba. Scene parsing through ade20k dataset. In *CVPR*, pages 633–641, 2017. 7

[58] Daquan Zhou, Bingyi Kang, Xiaojie Jin, Linjie Yang, Xiaochen Lian, Zihang Jiang, Qibin Hou, and Jiashi Feng. Deepvit: Towards deeper vision transformer. *arXiv preprint arXiv:2103.11886*, 2021. 1

A. Appendix

A.1. Pseudocode

This section describes the pseudo-code for the methods discussed in this paper. The pseudo-code for Raft-token-mixing Block is detailed in Listing 1, and the pseudo-code for Multi-scale Patch Embedding is detailed in Listing 2.

```
# b: size of mini -batch, h: height, w: width,
# c: channel, r: size of raft, o: c//r,
# e: expansion factor,
# x: input tensor of shape (h, w, c)

def __init__(self):
    self.lnv = nn.LayerNorm(c)
    self.lnh = nn.LayerNorm(c)
    self.fnv1 = nn.Linear(r * h, r * h * e)
    self.fnv2 = nn.Linear(r * h * e, r * h)
    self.fnh1 = nn.Linear(r * w, r * w * e)
    self.fnh2 = nn.Linear(r * w * e, r * w)

def forward(self, x):
    y = self.lnv(x)
    y = rearrange(y, 'b (h w) (r o) -> b (o w) (r
     h)')
    y = self.fcv1(y)
    y = F.gelu(y)
    y = self.fcv2(y)
    y = rearrange(y, 'b (o w) (r h) -> b (h w) (r
     o)')
    y = x + y
    y = self.lnh(y)
    y = rearrange(y, 'b (h w) (r o) -> b (o h) (r
     w)')
    y = self.fch1(y)
    y = F.gelu(y)
    y = self.fch2(y)
    y = rearrange(y, 'b (o h) (r w) -> b (h w) (r
     o)')
    return x + y
```

Listing 1. Pseudocode of raft-token-mixing block (Pytorch-like)

```
# b: size of mini-batch, h: height, w: width,
# kernels: list of kernel sizes for unfold.
#          e.g., [4, 8]

def __init__(self, in_channels, out_channels,
    kernels):
    mlp_in_channels = 0
    for k in kernels:
        mlp_in_channels += k ** 2
    mlp_in_channels *= in_channels
    self.embeddings = nn.ModuleList([
        nn.Sequential(*[nn.Unfold(
                kernel_size=k,
                stride=self.stride,
                padding=(k - self.stride) // 2),
            Rearrange("b c hw -> b hw c")
        ]) for k in kernels
    ])
    self.fc = nn.Linear(
        mlp_in_channels, out_channels
    )

def forward(self, input):
    b, _, h, w = input.shape
    outputs = []
    for emb in self.embeddings:
        output = emb(input)
        outputs.append(output)
    return self.fc(torch.cat(outputs, dim=2))
```

Listing 2. Pseudocode of multi-scale patch embedding (Pytorch-like)

A.2. Details of Architectures

RaftMLP The details of the architectures of RaftMLP-S, RaftMLP-M and RaftMLP-L used in this paper are details in Table 5.

Object Detection, Instance Segmentation and Semantic Segmentation For the RetinaNet [30] and Mask R-CNN [16] and Semantic FPN [23] we used, we consulted the results of [27], which is the same setup for ResNet, PureMLP, and ConvMLP, which are our comparison. The backbones we have experimented with are RaftMLP and Mixer-B/16. All of the architectures we have arranged use Feature Pyramid Network [29]. Therefore, we must clearly state what feature pyramid was input to these architectures from the backbones RaftMLP and Mixer-B/16. RaftMLP utilizes the output immediately after the first multi-scale patch embedding and the outputs of Level-2 to Level-4 as feature maps to be input to the detector and segmentor. Similarly, Mixer-B/16, along with RaftMLP, uses the output immediately after the patch embedding and the outputs of Block-4, Block-10, and Block-12 as before-mentioned feature maps.

A.3. Details of Quantitative Results

Object Detection and Instance Segmentation Table 6 contains the detailed results of the experiment for RetinaNet performed in Subsection 4.4, Table 7 includes the detailed results of the experiment for Mask R-CNN worked in Subsection 4.4. The results of RetinaNet are not doing as well overall as PureMLP, even with RaftMLP, which guarantees some spatial structure. In particular, it struggles to detect small objects. This result can be seen in A.5, where RaftMLP adds artifacts to the feature map, harming object detection.

Semantic Segmentation Table 8 contains the detailed results of the experiment performed in Subsection 4.5.

A.4. Qualitative Results

Object Detection and Instance Segmentation Figure 7a shows the ground truth for an image of MS COCO validation dataset. Figure 7b shows the inference result for RetinaNet with ResNet-50 as the backbone to be installed in `mmdetection`, and Figure 7c, 7d, 7e, and 7f inference results for the four RetinaNets trained in Subsection

4.4. Figure 7g shows the inference result for Mask R-CNN with ResNet-50 as the backbone to be installed in `mmdetection`, and Figure 7h, 7i, 7j, and 7k inference results for the four Mask R-CNNs trained in Subsection 4.4. Despite the lack of precision, the figures reveal that results of Global MLP-based models for the object detection and instance segmentation tasks are satisfactory.

Semantic Segmentation Figure 8a presents an image with ADE20k validation dataset overlaid with its ground truth. Figure 8b shows the inference results of the model applying ResNet-50, which `mmsegmentation` provides, as the backbone of the Semantic FPN. Figures 8c, 8d, 8e, and 8f show the inference results for the four models we trained in Subsection 4.5 experiment.

A.5. Visualization

We used an image with ImageNet to visualize and compare its feature map. The image used as input was the ferret image on the left of Figure 9, which was input to pretrained ResNet-50, Mixer-B/16, and RaftMLP-M. Some of the outputs of the intermediate layers are summarized on the right side of Figure 9. For ResNet-50, we used the output of layers 1 through 4; for Mixer-B/16, we used the output of Blocks 2, 4, 10, and 12; for RaftMLP-M, we used the output of each Level. We have also included further intermediate layer outputs for the three models, see Figure 10, 11, 12, and 13 for Resnet-50, Figure 14, 15, 16 and 17 for Mixer-B/16, and Figure 18, 19, 20, and 21 for RaftMLP-M.

As mentioned in Section 5, the appearance of features in the middle layer of global MLP-based models is different from that of the convolutional base represented by ResNet. We believe this is why global MLP-based models do not perform well when selected as the backbone of existing architectures for object detection, instance segmentation, and semantic segmentation. The feature map of RaftMLP-M is different from that of ResNet in that the lower layers have feature maps that capture the features of the ferret. In contrast, the upper layers have feature maps with visible artifacts of vertical and horizontal lines. The feature maps of Mixer-B/16 do not capture the features of the ferret, and they are overall shuffled and have many similar feature maps. Tasks such as object detection, semantic segmentation, or even image generation will require innovations specific to global MLP-based models. The occurrence of artifacts might have a minor impact on classification, where global average pooling is used. However, for tasks such as segmentation and image generation, it becomes a severe problem. Hence, it will be necessary to design architectures and loss functions that do not emit this artifact. Or else, convolution-based methods such as RetinaNet, Mask R-CNN, and Semantic FPN may be insufficient to recover the whole shuffled information by global MLP-based models. To recover the global shuffled information by the global MLP-based model, global MLP-based models may lack a module that can capture the global relations, such as self-attention modules and token-mixing blocks.

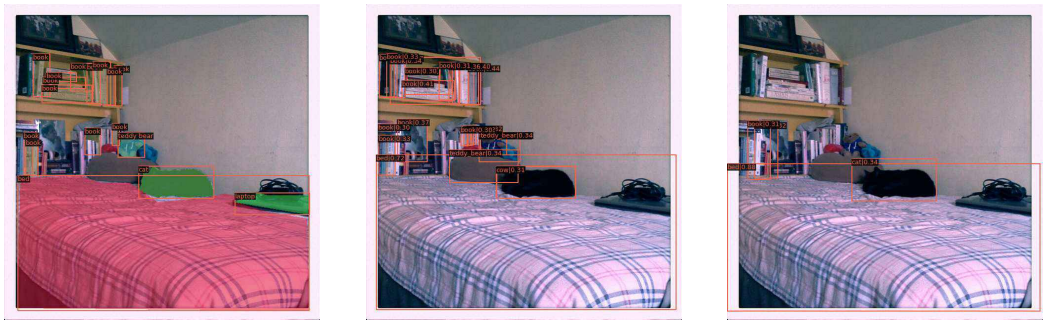

(a) Ground Truth (b) RetinaNet—ResNet-50 (c) RetinaNet—Mixer-B/16

(d) RetinaNet—RaftMLP-S (e) RetinaNet—RaftMLP-M (f) RetinaNet—RaftMLP-L

(g) Mask R-CNN—ResNet-50 (h) Mask R-CNN—Mixer-B/16 (i) Mask R-CNN—RaftMLP-S

(j) Mask R-CNN—RaftMLP-M (k) Mask R-CNN—RaftMLP-L

Figure 7. Qualitative results of object detection and instance segmentation

(a) Ground Truth (b) Semantic FPN—ResNet-50 (c) Semantic FPN—Mixer-B/16

(d) Semantic FPN—RaftMLP-S (e) Semantic FPN—RaftMLP-M (f) Semantic FPN—RaftMLP-L

Figure 8. Qualitative results of semantic segmentation

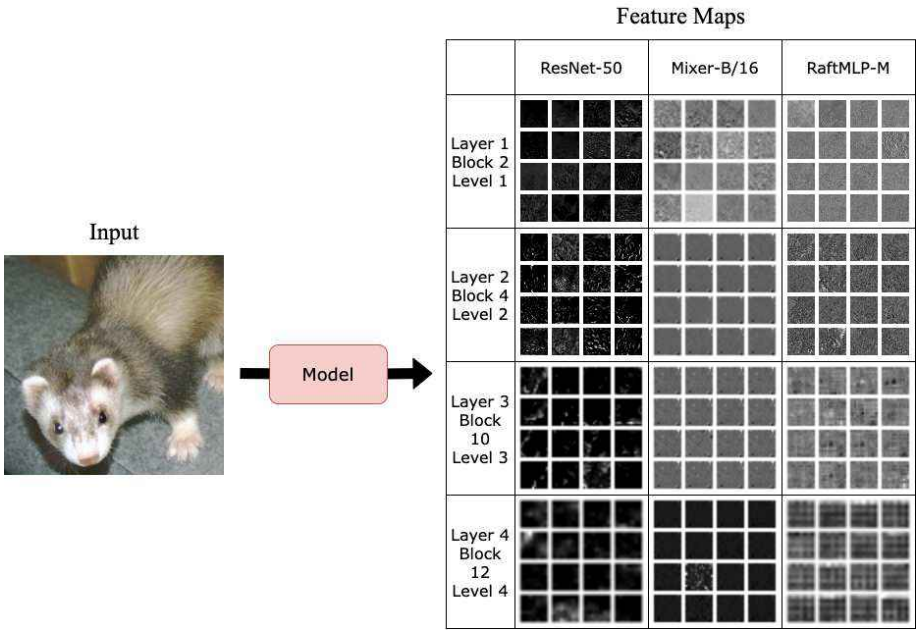

Figure 9. Summary of the comparison of ResNet-50, Mixer-B/16, and RaftMLP-M intermediate layer feature maps

Table 5. Specific settings on the model architectures of hierarchy RaftMLP in different scales. l denotes level and c'_l denotes the number of basic channels in RaftMLP for level l.

Model	RaftMLP-S		RaftMLP-M		RaftMLP-L	
Level	Block	Setting	Block	Setting	Block	Setting
$l = 1$	RaftMLP×2	$c'_1 = 64$	RaftMLP×2	$c'_1 = 96$	RaftMLP×2	$c'_1 = 128$
$l = 2$	RaftMLP×2	$c'_2 = 128$	RaftMLP×2	$c'_2 = 192$	RaftMLP×2	$c'_1 = 192$
$l = 3$	RaftMLP×6	$c'_3 = 256$	RaftMLP×6	$c'_3 = 384$	RaftMLP×6	$c'_1 = 512$
$l = 4$	RaftMLP×2	$c'_4 = 512$	RaftMLP×2	$c'_4 = 768$	RaftMLP×2	$c'_1 = 1024$

Table 6. Comparison of RetinaNet metrics trained on MS COCO with each ResNet, PureMLP, ConvMLP, RaftMLP, and Mixer as the backbone.

Backbone	#MParams	AP^b	AP^b_{50}	AP^b_{75}	AP^b_S	AP^b_M	AP^b_L
ResNet-18 [17, 27]	21.3	31.8	49.6	33.6	16.3	34.3	43.2
PureMLP-S [27]	17.6	27.1	44.2	28.3	13.6	29.2	36.4
ConvMLP-S [27]	18.7	37.2	56.4	39.8	20.1	40.7	50.4
RaftMLP-S	19.6	17.7	33.3	16.5	4.5	14.1	32.4
ResNet-50 [17, 27]	37.7	36.3	55.3	38.6	19.3	40.0	48.8
PureMLP-M [27]	25.9	28.0	45.6	29.0	14.5	29.9	37.8
ConvMLP-M [27]	27.1	39.4	58.7	42.0	21.5	43.2	52.5
RaftMLP-M	27.1	19.3	36.3	17.8	5.2	15.9	35.1
ResNet-101 [17, 27]	56.7	38.5	57.8	41.2	21.4	42.6	51.1
PureMLP-L [27]	50.1	28.8	46.8	29.9	15.0	31.0	38.4
ConvMLP-L [27]	52.9	40.2	59.3	43.3	23.5	43.8	53.3
RaftMLP-L	52.9	19.5	36.8	18.1	5.0	16.1	35.4
Mixer-B/16 [43]	70.3	10.7	20.0	10.1	0.1	6.7	25.8

Table 7. Comparison of Mask R-CNN metrics trained on MS COCO with each ResNet, PureMLP, ConvMLP, RaftMLP and Mixer as the backbone.

Backbone	#MParams	AP^b	AP^b_{50}	AP^b_{75}	AP^m	AP^m_{50}	AP^m_{75}
ResNet-18 [17, 27]	31.2	34.0	54.0	36.7	31.2	51.0	32.7
PureMLP-S [27]	27.5	25.1	45.1	25.1	25.0	42.8	26.0
ConvMLP-S [27]	28.7	38.4	59.8	41.8	35.7	56.7	38.2
RaftMLP-S	29.5	21.8	40.2	21.0	19.7	36.5	19.1
ResNet-50 [17, 27]	44.2	38.0	58.6	41.4	34.4	55.1	36.7
PureMLP-M [27]	35.8	25.8	46.1	25.8	25.6	43.5	26.5
ConvMLP-M [27]	37.1	40.6	61.7	44.5	37.2	58.8	39.8
RaftMLP-M	40.9	23.4	42.5	22.7	21.1	38.8	20.8
ResNet-101 [17, 27]	63.2	40.4	61.1	44.2	36.4	57.7	38.8
PureMLP-L [27]	59.5	26.5	45.0	27.4	26.7	47.5	26.8
ConvMLP-L [27]	62.2	41.7	62.8	45.5	38.2	59.9	41.1
RaftMLP-L	55.5	24.2	43.9	23.7	21.6	39.7	23.7
Mixer-B/16 [43]	79.8	11.9	22.8	11.2	9.5	19.1	8.5

Table 8. Comparison of Semantic FPN metrics trained on MS COCO with each ResNet, PureMLP, ConvMLP, RaftMLP and Mixer as the backbone.

Backbone	#MParams	mIoU
ResNet-18 [17, 27]	15.5	32.9
Pure-MlP-S [27]	11.6	23.9
ConvMLP-S [27]	12.8	35.8
RaftMLP-S	13.6	30.7
ResNet-50 [17, 27]	28.5	36.7
Pure-MlP-M [27]	19.9	25.2
ConvMLP-M [27]	21.1	38.6
RaftMLP-M	25.0	32.3
ResNet-101 [17, 27]	47.5	38.8
Pure-MlP-L [27]	43.6	26.3
ConvMLP-L [27]	46.3	40.0
RaftMLP-L	39.6	33.3
Mixer-B/16 [43]	63.9	28.1

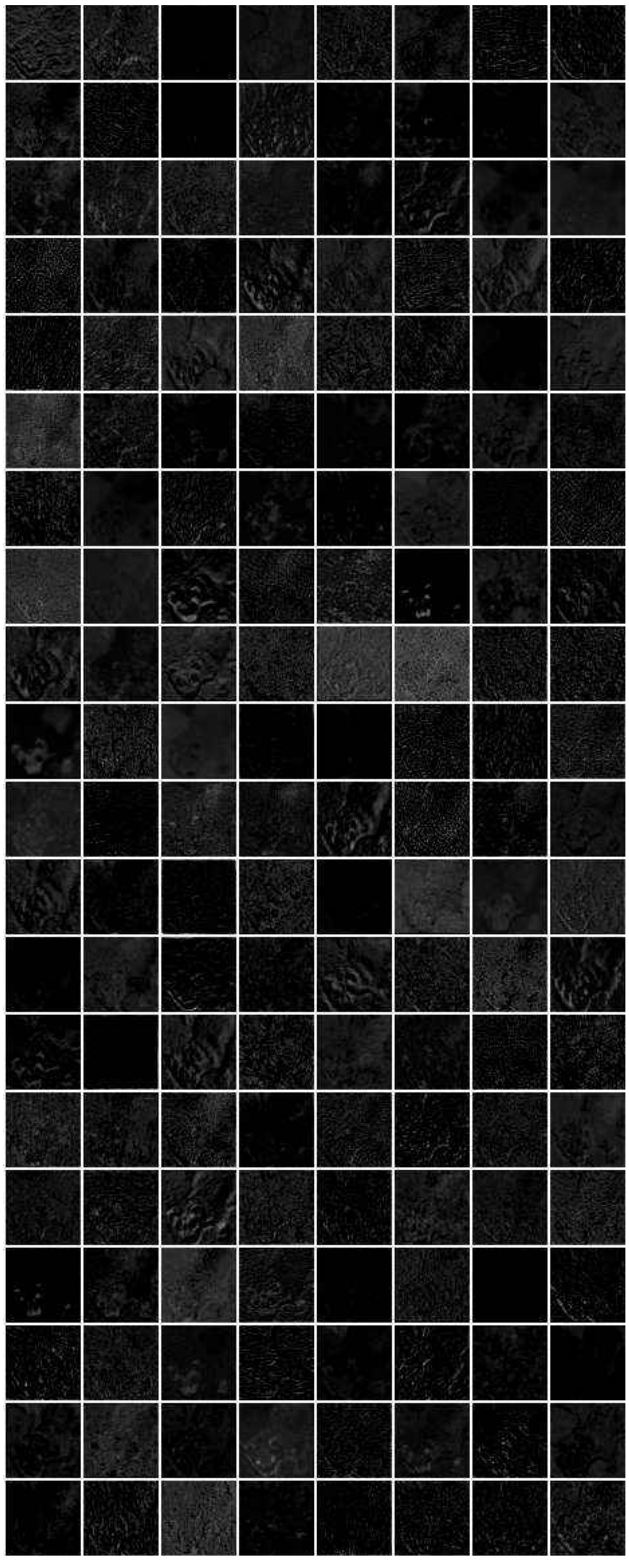

Figure 10. Part of the feature maps output from Layer-1 of ResNet-50 with the ferret images as input

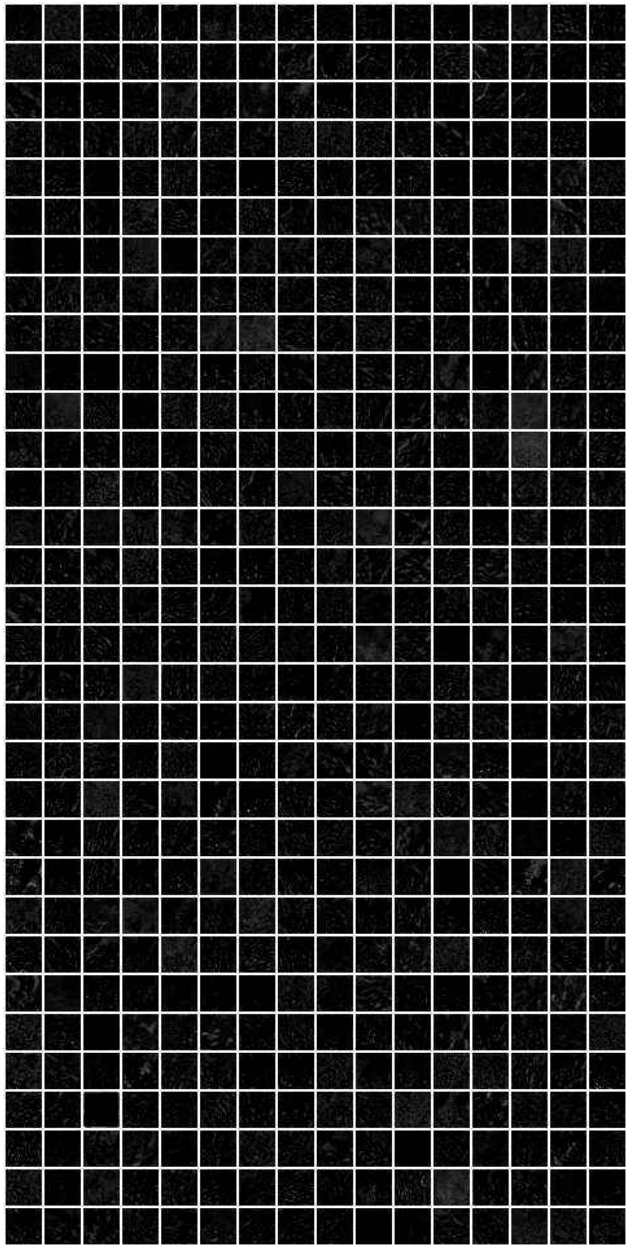

Figure 11. All the feature maps output from Layer-2 of ResNet-50 with the ferret images as input

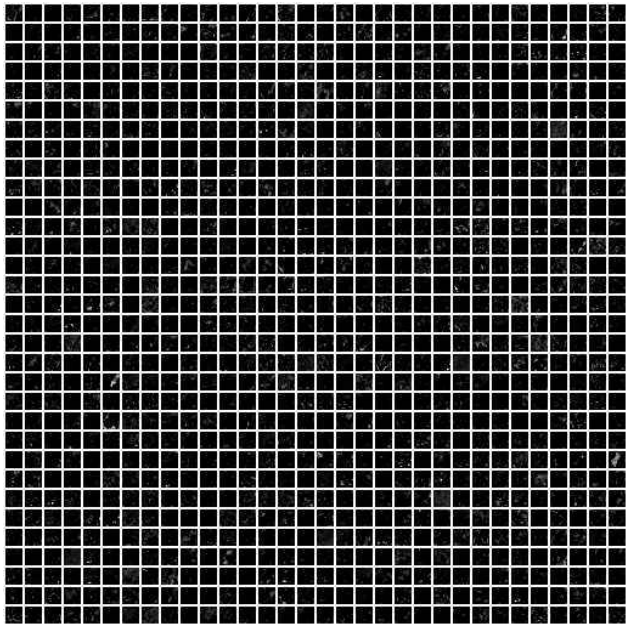

Figure 12. All the feature maps output from Layer-3 of ResNet-50 with the ferret images as input

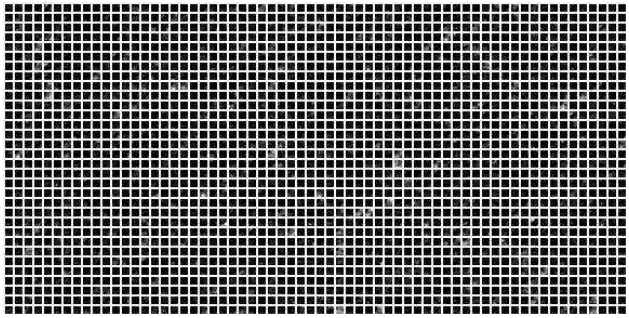

Figure 13. All the feature maps output from Layer-4 of ResNet-50 with the ferret images as input

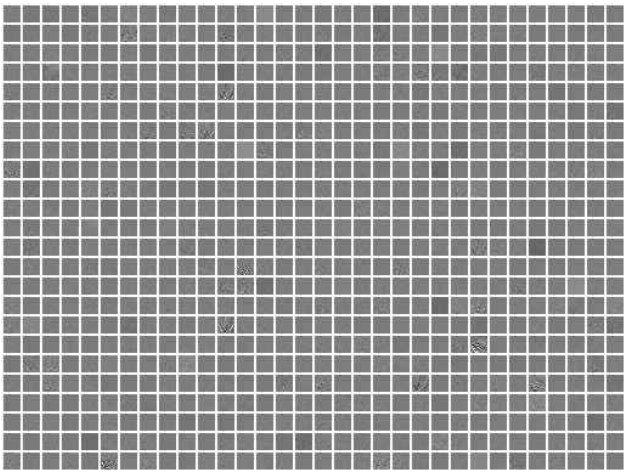

Figure 14. All the feature maps output from Block-2 of Mixer-B/16 with the ferret images as input

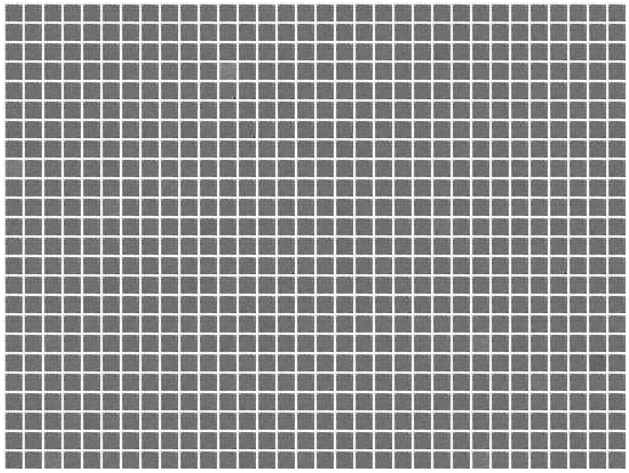

Figure 15. All the feature maps output from Block-4 of Mixer-B/16 with the ferret images as input

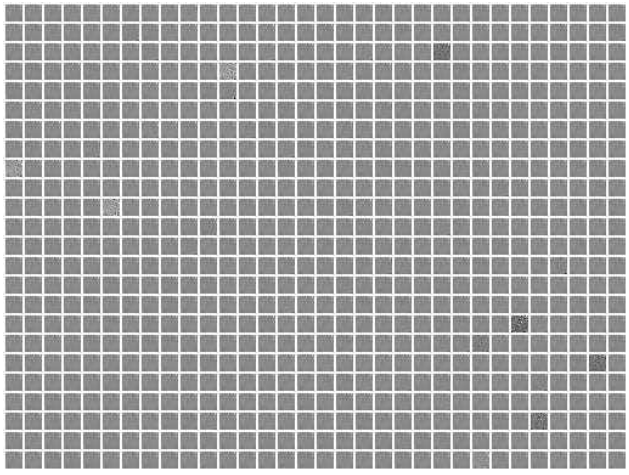

Figure 16. All the feature maps output from Block-10 of Mixer-B/16 with the ferret images as input

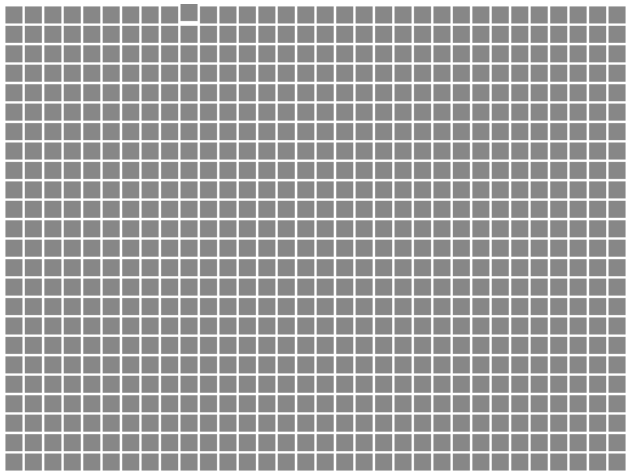

Figure 17. All the feature maps output from Block-12 of Mixer-B/16 with the ferret images as input

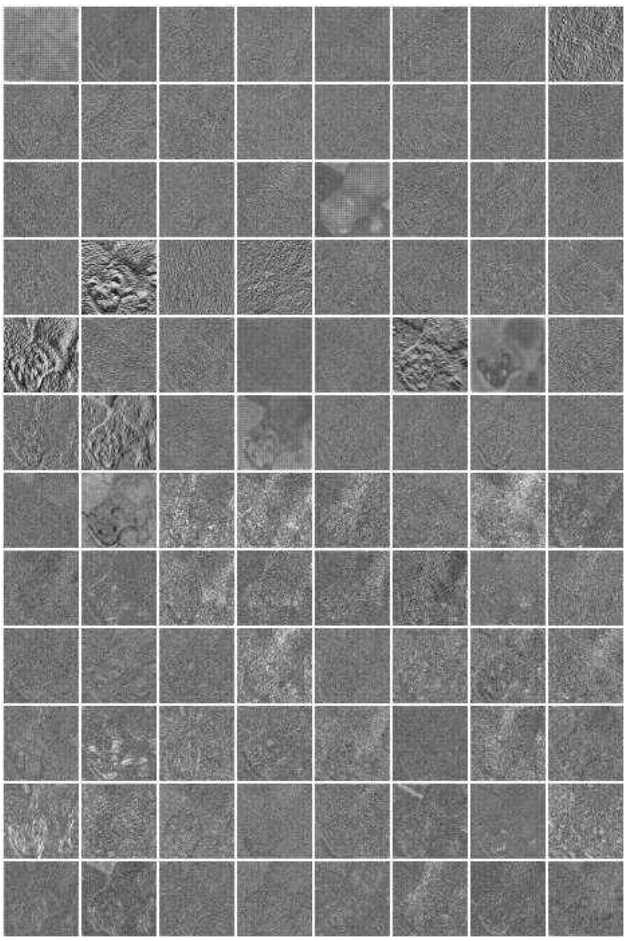

Figure 18. All the feature maps output from Level-1 of RaftMLP-M with the ferret images as input

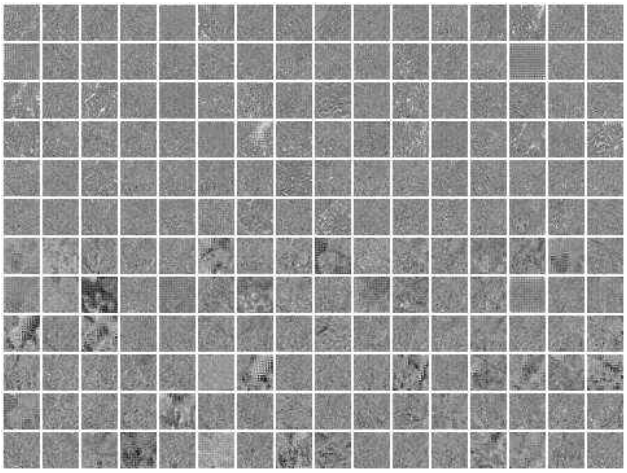

Figure 19. All the feature maps output from Level-2 of RaftMLP-M with the ferret images as input

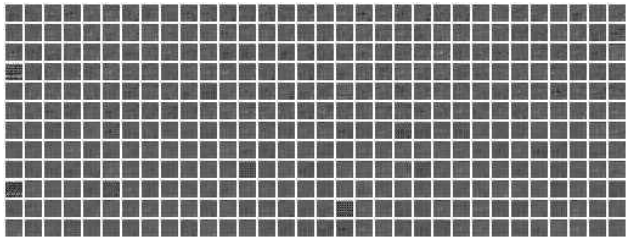

Figure 20. All the feature maps output from Level-3 of RaftMLP-M with the ferret images as input

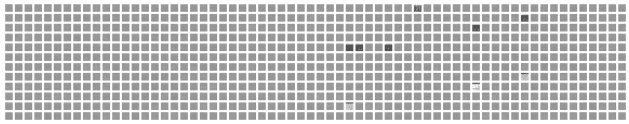

Figure 21. All the feature maps output from Level-4 of RaftMLP-M with the ferret images as input